



Contents lists available at ScienceDirect

Journal of Power Sources

journal homepage: www.elsevier.com/locate/jpowsour

4D-resolved physical model for Electrochemical Impedance Spectroscopy of $\text{Li}(\text{Ni}_{1-x-y}\text{Mn}_x\text{Co}_y)\text{O}_2$ -based cathodes in symmetric cells: Consequences in tortuosity calculations

Abbos Shodiev^{a,b,1}, Emiliano N. Primo^{a,b,1}, Mehdi Chouchane^{a,b}, Teo Lombardo^{a,b},
Alain C. Ngandjong^{a,b}, Alexis Rucci^{a,b}, Alejandro A. Franco^{a,b,c,d,*}

^a Laboratoire de Réactivité et Chimie des Solides (LRCS), UMR CNRS 7314, Université de Picardie Jules Verne, HUB de l'Energie, 15 rue Baudelocque, 80039, Amiens Cedex, France

^b Réseau sur le Stockage Electrochimique de l'Energie (RS2E), FR CNRS 3459, HUB de l'Energie, 15 rue Baudelocque, 80039, Amiens Cedex, France

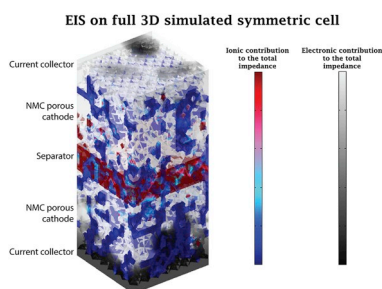
^c ALISTORE-European Research Institute, FR CNRS 3104, HUB de l'Energie, 15 rue Baudelocque, 80039, Amiens Cedex, France

^d Institut Universitaire de France, 103 Boulevard Saint Michel, 75005, Paris, France

HIGHLIGHTS

- A 4D physical model was used to simulate EI spectra of NMC porous cathodes.
- The model considers explicitly the three electrode phases and different physics.
- The main features of the EI spectra were analyzed and compared with experiments.
- Complex interplay between electronic and ionic conductivities were found.
- The study allowed to perform a discussion on the EIS-based tortuosity calculation.

GRAPHICAL ABSTRACT



ARTICLE INFO

Keywords:

Lithium ion batteries
NMC cathodes
Symmetric cell
Electrochemical impedance spectroscopy
4D-resolved physical modeling

ABSTRACT

Electrochemical impedance spectroscopy (EIS) constitutes an experimental technique used for the characterization of Lithium Ion Battery (LIB) porous electrodes tortuosities. For the first time, a 4D (3D in space + time) physical model is proposed to simulate EIS carried out on NMC porous cathodes, derived from the simulation of their manufacturing process, in symmetric cells. EIS is simulated by explicitly considering the NMC active material, carbon-binder domains (CBD) and pores as spatially-resolved separated phases and assuming different physics for each of them. The calculated impedance responses are compared with *in house* experimental results coming from NMC-based cathodes prepared in a similar way. We investigate the influence of the physics assumed to describe the CBD behavior, the conductivity of the different solid phases and electrolyte, the relative amount of NMC and CBD and the impact of calendaring on the EI spectra, and we compare the results with the experimental EIS measurements. This methodology allows to understand the limitations of using EIS, electric circuit models and homogenized physical models for the determination of the tortuosity factor of NMC-based cathodes,

* Corresponding author. Laboratoire de Réactivité et Chimie des Solides (LRCS), UMR CNRS 7314, Université de Picardie Jules Verne, HUB de l'Energie, 15 rue Baudelocque, 80039, Amiens Cedex, France.

E-mail address: alejandro.franco@u-picardie.fr (A.A. Franco).

¹ These authors contributed equally to this work.

<https://doi.org/10.1016/j.jpowsour.2020.227871>

Received 5 December 2019; Received in revised form 24 January 2020; Accepted 7 February 2020

0378-7753/© 2020 The Authors. Published by Elsevier B.V. This is an open access article under the CC BY-NC-ND license

(<http://creativecommons.org/licenses/by-nc-nd/4.0/>).

revealing a complex interplay between the conductivity of the solid phases, the electrolyte properties and the cathode meso/microstructure.

1. Introduction

The development of Lithium-Ion Battery (LIB) started during the oil crisis in the 1970s. Researching on materials for semiconductors, Stanley Whittingham designed an energy-rich lithium battery that was subsequently refined by his fellow Nobel laureates John B. Goodenough and Akira Yoshino, who improved the technology by replacing the cathode and anode with lithium cobalt oxide and graphite, respectively [1]. Since the first commercial LIB in 1991, the world has seen a boom in portable electronics, long-range electric vehicles and the possibility of acting as an accumulator for renewable sources such as solar and wind power. In this sense, optimization studies are still required to improve LIB electrochemical performance and to decrease their cost. Generally, the former depends on the chemistry of the active materials and electrode mesostructure characterized by its porosity (ϵ) and pore size distribution, electronic and ionic conductivity and geometrical tortuosity (or tortuosity factor). Except for the latter, all the other properties can be determined experimentally through simple characterization techniques. On the contrary, there is not a direct way to determine the tortuosity, which expresses the ratio of the average pore length between two random points within an electrode mesostructure and the geometrical shortest path between the points (in Cartesian coordinates, a straight line). This is an important property controlling the effective transport capabilities towards lithium ions in porous electrodes. Recently, Tjaden et al. have thoroughly reviewed different definitions of tortuosity and measurement schemes allowing to derive its value and made an analysis of the limitations of each one [2].

In the battery field, one of the most straightforward ways of obtaining the value of the tortuosity factor (τ) is through the MacMullin number (N_M), where $N_M = \tau/\epsilon = X/X_{eff}$ being X the electrolyte bulk conductivity or diffusion coefficient and the subscript *eff* refers to its effective value within the porous electrode [3–5]. The effective ionic conductivity of electrodes can be determined through Electrochemical Impedance Spectroscopy (EIS) using the so-called transmission line model (TLM) [6], through which the ionic resistance of the electrolyte in the porous structure is obtained in the mid-frequencies 45° slope region. Although this constitutes a rather simple way to estimate how the electrode morphological properties affect the τ of the porous mesostructure, the main limitation of this approximation is that it considers all the pores as a collection of parallel identical cylindrical reservoirs of electrolyte with constant conductivity through the z direction, i.e. the electrode thickness [7]. Several authors have addressed this issue by using more complicated TLMs and/or explicit transport equations to describe the ionic and electric current in the porous electrode. Within the first approach, embedded TLMs were used for modelling fractal distribution of pores [8], a TLM with a normal distribution of pore radius and density per unit surface was added to study the impact of pore size distribution [9] and a multiscale TLM-electrical circuit model was used to distinguish nano- and micro-scale interparticle pore contributions [10]. As to the second approach, Cooper et al. developed a series of steady-state ion transport equations in the frequency domain applied to several 2D pore morphologies and pseudo-3D and 3D electrode structures [11]. Kant and Singh proposed a theory that combines the diffuse layer dynamics at the electrode mesoscale, through the Debye-Falkenhagen model of electrical double layer relaxation, and micropores dynamics by employing a TLM [7]. This model was applied to arbitrary shaped mesostructures with embedded heterogeneous micropores. Although they provided valuable insights as to how the EIS profile changes when taking into account more complicated pore size distributions, they all simplify the electrode micro/mesostructure into arbitrary morphologies (in the case of electrical circuit studies they

actually do not take into account any electrode morphology) and/or do not explicitly consider all the phases present in a conventional electrode, i.e., the active material, the conductive carbon, the binder and the void between them that is filled with electrolyte. It is worth mentioning that despite its limitations, TLMs have been applied for studying τ and electrolyte ionic resistance within the pores (R_{ion}) in graphite-based anodes [12–14], LiNiO_2 [15], LiFePO_4 [3] and $\text{LiNi}_{1/3}\text{Mn}_{1/3}\text{Co}_{1/3}\text{O}_2$ [3] cathodes.

It is also common to see in literature Newman-type 1D or pseudo-2D physical models to simulate LIB electrode performance, which are based on the homogenization of the active material (AM) and carbon-binder domain (CBD) into one solid phase [12,16–18]. Such homogenization does not allow to investigate how the spatial location of the carbon-binder domain (CBD) and different interfaces affects the overall electrode performance.

In a recent publication we have reported a 4D (3D in space + time) LIB cell physical model which captures the impact of the spatial location of CBD and interfaces on the overall electrochemical performance upon discharge [19,20]. Our model allows to minimize input parameters and geometrical assumptions (by considering explicitly AM, CBD and pore phases) and to carry out very precise studies about the electrode texture [20].

In the present work an extension of that model is used to investigate EIS features of LIB porous electrodes characterized in a symmetric cell configuration. To the best of our knowledge, the use of multiphase geometries for EIS simulations is introduced for the first time ever. Here, the porous electrode consists of three distinct phases: the NMC active material, the CBD and the void between them, which is filled with the electrolyte. This gives several advantages, namely, the possibility of assigning different physics to each phase and taking into account explicitly the double layer contribution of each one [19,21,22]. First, we introduce the model main features and assumptions. Second, a detailed analysis of the EIS spectra main features is carried out, by changing the physics of the different phases and comparing with *in house* experimental results. Finally, a general discussion is performed around the limitation of this EIS methodology for the calculation of τ in porous electrodes. We believe that, because of the explicit consideration of the electrode micro/mesostructure, our modeling approach can be used to decrease the gap between modeling and experiment and to help resolving existing controversies in regards of the experimental EIS data interpretation.

2. Theory

2.1. Electrode structures generation

The workflow for the generation of the 3D-resolved electrode mesostructures has been already presented in our previous works [23,24]. Briefly, the generation of the electrodes starts by modeling the slurry preparation through a Coarse-Grained Molecular Dynamics (CGMD) simulation. At this stage, beads representing NMC and carbon-binder domain (CBD) particles are randomly placed in the simulation box and then allowed to equilibrate through a MD simulation (NPT ensemble) [23]. The force field used to model the particles interactions is derived from a combination of Lennard-Jones and Granular-Hertzian potentials and was parametrized and validated with experimental NMC slurries. The drying step was performed by shrinking through MD simulation (at NPT) the effective CBD particles to a final diameter lower than the one in the slurry state, in order to mimic the loss of the solvent. Further information and data about CGMD simulations can be found in the Supporting Information, section 1. At the second stage, post-CGMD obtained

electrode structures were meshed by using our voxelization algorithm INNOV in MATLAB environment and imported into Comsol Multiphysics 5.4 software [19]. The last stage is to apply appropriate material properties and physical models to the 3D multi-phase mesh and to calculate the EI spectra by using Comsol Multiphysics software.

2.2. Electrochemical model

The imported volumetric multi-phase mesh consists of five subdomains: NMC and CBD particles, separator, current collector and electrolyte. The full physics behind the 3D EIS model and geometry subdomains are provided in Fig. 1 and Table 1.

2.2.1. Electrode level

The AM particles consist of a solid matrix, where the Ohm's law is used to describe the electronic conductivity (Eq. (2)). Since the AM specific surface area is normally two orders of magnitude lower than the one of carbon additive, the current density coming from the double layer formation comes mainly from the latter. Therefore, it was assumed that the NMC surface in contact with the electrolyte does not form a double layer (Eqs. (18) and (19)). Moreover, and for simplifying the model, no interfacial resistance between AM and CBD was considered.

It is known that conductive carbon black is added to ensure good electrical connection between the current collector and the resistive NMC AM phase [25,26]. Furthermore, being a small and high surface-to-volume ratio material, it contributes to a large extent to the final electrode ε and τ . In our model, the CBD particle is a mixture of solid electronic conductor (with a certain volume fraction) and electrolyte permeable phase in order to mimic the microporosity present in carbon/binder mixtures. On one hand, it is known that the binder allows the transport of ions and swells upon impregnation with the electrolyte [27]. On the other, the carbon additive particles are normally of ~ 50 nm diameter, generating an interconnected porous hierarchical microstructure within the electrode. In the case of CBD-solid subdomain, modified Ohm's law was used. The electrolyte-permeable subdomain was represented as a phase with 20% of its volume accessible to the electrolyte (Eqs. (10) and (11)), with effective σ_{el}^{eff} and D_{el}^{eff} corrected by the Bruggeman relation, and 80% of it as conductive solid (Eq. (13)). As

mentioned above double layer formation takes place on the surface of CBD so a capacitive double layer current density term was included in the CBD-electrolyte interphase (Eq. (20)), assuming its formation is homogenous. A volumetric double layer was also added to take into account the contribution of the effective microporosity of the CBD phase (Eq. (20)).

2.2.2. Separator level

The used Targary PE 16A separator 3D microstructure was taken from open source tomography data [28]. The information about geometry and ε of separator are given in Table 2 and the meshed structure is shown in the Supporting Information, section 3.

2.2.3. Electrolyte level

One of the assumptions of the model is that the electrolyte fills the void between all the solid domains. The electrolyte is non-intercalating in order to avoid faradaic processes, and diluted to keep as small as possible the ratio between the ionic and electronic resistance [3]. Nernst-Planck equations are used to describe ionic transport in the diluted electrolyte (Eqs. (3) and (4)) [29,30]. It was assumed constant temperature across the cell and no convection taking place. For the electrolyte subdomain within CBD, transport parameters were corrected by using the effective Bruggeman relation (Eqs. (10) and (11)).

2.2.4. Current collector level

The current collector consists of a full solid domain, where the Ohm's law for electronically conducting materials is used to describe its properties (Eqs. (15) and (16)). In this work no electrode-current collector interface resistance was considered.

2.3. Simulation procedure

The EI spectra were calculated in Comsol Multiphysics 5.4 environment, using the Battery and the Transport of Diluted species modules [31]. The impedance was calculated at 10 frequencies per decade, ranging from 1 to 10^7 Hz. A sinusoidal perturbation of 10 mV was applied and the resulting current output model equations were linearized. By applying a Laplace transformation, the response was expressed

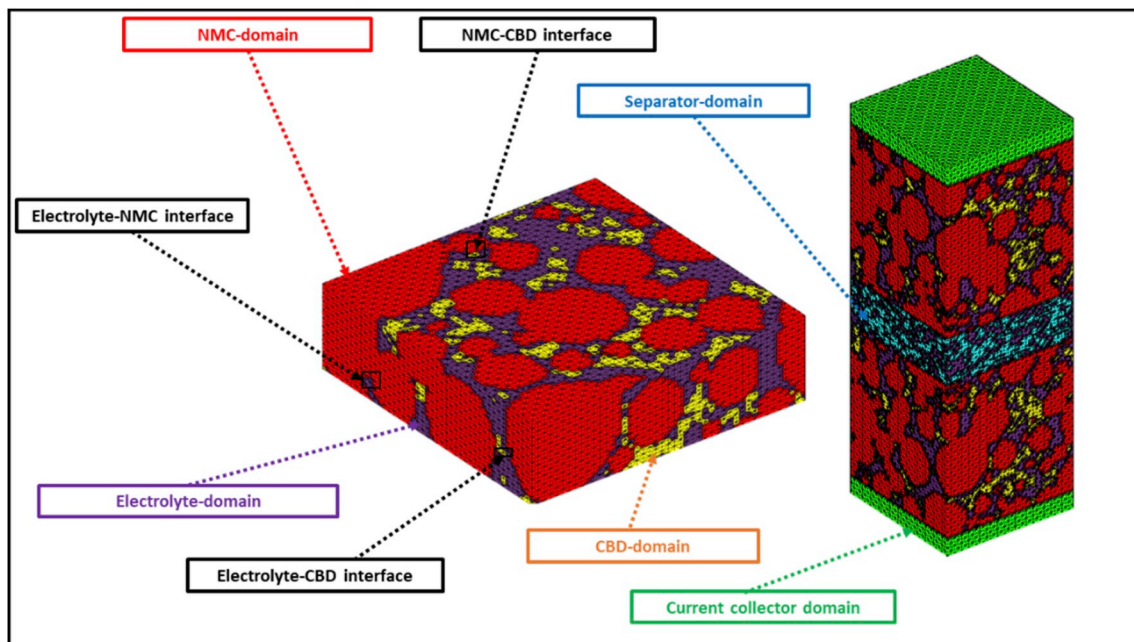


Fig. 1. Scheme of the simulated symmetric cell.

Table 1

List of equations for the EIS modeling.

| NMC-domain governing equations | |
|--|---|
| $\nabla(j_{NMC}) = 0$ | (1) Bulk electrode current source |
| $-K_{NMC} \cdot \nabla \varphi_{NMC} = j_{NMC}$ | (2) Ohm's law for electronically conducting matrix |
| Electrolyte-domain governing equations | |
| $\frac{\partial C_{el}}{\partial t} = -\nabla(N_{el})$ | (3) Diluted solution binary electrolyte mass transport |
| $\left(-D_i \nabla C_i - \frac{D_i}{RT} FC_i \nabla \varphi_{el}\right) = N_i$ | (4) Mass transport in electrolyte due to diffusion and migration |
| $\nabla(j_{el}) = 0$ | (5) Bulk electrolyte current source |
| $j_{el} = -\sigma_{el} \cdot \nabla \varphi_{el}$ | (6) Ohm's law for diluted solution binary electrolyte |
| CBD-domain governing equations | |
| $\frac{\partial C_{el}}{\partial t} = -\nabla(N_{el})$ | (7) Diluted binary solution electrolyte mass transport in the CBD domain |
| $j_{el} = -\sigma_{el} \cdot \nabla \varphi_{el}$ | (8) Ohm's law for diluted binary solution of the electrolyte in the CBD |
| $\left(-D_i^{eff} \nabla C_i - \frac{D_i^{eff}}{RT} FC_i \nabla \varphi_{el}\right) = N_i$ | (9) Mass transport of the electrolyte due to diffusion and migration in the CBD |
| $D_{el}^{eff} = \varepsilon_{el}^{1.5} D_{el}$ | (10) Effective Bruggeman diffusion parameter of the electrolyte inside the CBD |
| $\sigma_{el}^{eff} = \varepsilon_{el}^{1.5} \sigma_{el}$ | (11) Effective Bruggeman conductivity parameter of the electrolyte inside the CBD |
| $-K_{CBD}^{eff} \cdot \nabla \varphi_{CBD} = j_{CBD}$ | (12) Ohm's law for solid effective conducting matrix of CBD |
| $K_{CBD}^{eff} = \varepsilon_{el}^{1.5} K_{CBD}$ | (13) Effective Bruggeman solid conductivity parameter of CBD |
| $\nabla(j_{CBD}) = 0$ | (14) Bulk CBD solid current source |
| Current collector domain equations | |
| $\nabla(j_{cc}) = 0$ | (15) Bulk current collector current source |
| $-K_{cc} \cdot \nabla \varphi_{cc} = j_{cc}$ | (16) Ohm's law for electronically conducting matrix in the current collector |
| Electrolyte-NMC interface | |
| $-n \cdot j_{el} = 0$ | (17) No current density flow between NMC and electrolyte phase |
| $-n \cdot j_{NMC} = 0$ | (18) |
| Electrolyte-CBD interface | |
| | Double layer current |

Table 1 (continued)

| $\left(\frac{\partial (\varphi_{CBD} - \varphi_{el})}{\partial t}\right) \cdot (C_{dl}) = j_{dl}$ | (19) |
|---|--|
| CBD volumetric double layer | |
| $j_{dl} \cdot A_{dl} = j_{V,dl}$ | (20) Total volumetric double layer current |
| Applied perturbation | |
| $\varphi_{app} = \Delta \varphi e^{-i\omega t} = 10 \text{ mV}$ | (21) |
| Electric Ground | |
| $\varphi_s = 0$ | (22) |
| Formulation of the variables in the frequency domain | |
| $a = a_0 + Re(\tilde{a} \cdot e^{2\pi f \cdot u})$ | (23) |

in the frequency domain. The EIS 4D heterogeneous model simulations were performed using an Intel® Xeon® E5-2609 CPU @ 1.9 GHz (2 processors) with 32 GB of RAM and Intel® Xeon® E5-4627 Cache @ 3.30 GHz with 264 GB of RAM. Each simulation took approximately between 8 and 20 h depending on input parameters and the electrode structure. All the cell parameters and constants used for the EIS simulation are listed in Table 2.

For the calculation of τ on simulated electrodes using GeoDict® software the readers are referred to section 2 in the Supporting Information.

3. Experimental methodology

LiNi_{1/3}Mn_{1/3}Co_{1/3}O₂ (NMC) was supplied by Umicore. C-ENERGY™ super C65 carbon black was supplied by IMERYS. Solef™ Polyvinylidene fluoride (PVdF) was purchased from Solvay and N-methylpyrrolidone (NMP) from BASF. Tetrabutylammonium perchlorate (TBAClO₄) was from Alfa Aesar. All the other reagents were battery grade and were used without further purification.

The slurry solid components NMC, C65 and PVdF were premixed with a soft blender. Afterwards, NMP was added until reaching the desired ratio between solvent and solid components. The total mass of solid components was always 65 g. The mixture was performed in a Dispermat CV3-PLUS high-shear mixer for 2 h in a water-bath cooled recipient at 25 °C. The slurry was coated over a 22 µm thick Aluminum current collector using a comma-coater prototype-grade machine. The electrodes analyzed in this work were NMC 96% - C 2% - PVdF 2%, NMC 95% - C 2.5% - PVdF 2.5% and NMC 94% - C 3% - PVdF 3%. The thicknesses and porosities for each electrodes are, respectively, 174.7 ± 0.9 µm/45 ± 2%, 169 ± 1 µm/46 ± 2% and 164 ± 3 µm/49 ± 2%.

All EIS tests were performed in 2035 coin cells assembled in a dry room (H₂O < 15 ppm). NMC cathodes were punched into 13 mm electrodes and were assembled into the coin cells (both at the positive and negative side) using Celgard 2500 as separator (thickness = 25 µm, porosity = 55%). The electrolyte was a 10 mM TBAClO₄ solution, prepared in a 1:1 wt mixture of ethylenecarbonate:dimethylcarbonate. The EIS were performed with a MTZ-35 impedance analyzer (BioLogic, Seyssinet-Pariset, France) in the range of 10⁻¹ – 10⁵ Hz with a potential perturbation of 10 mV. All measurements were carried out at 25 ± 1 °C.

Table 2

Symmetric cell dimensions and model inputs. The 3D meshed structures of each symmetric cell can be found in the Supporting Information, section 3.

| | |
|--|--|
| AM 96% - CBD 4% symmetric cell dimensions | |
| Simulation Box | $99.60 \times 35.3 \times 35.30 \mu\text{m}^3$ (293172 tetrahedrons in mesh) |
| Electrode | $38.8 \times 35.3 \times 35.3 \mu\text{m}^3$ |
| Current collector | $5 \times 35.3 \times 35.30 \mu\text{m}^3$ |
| Separator | $12 \times 35.3 \times 35.3 \mu\text{m}^3$ |
| AM 95% - CBD 5% symmetric cell dimensions | |
| Simulation Box | $92 \times 37.8 \times 37.8 \mu\text{m}^3$ (215607 tetrahedrons in mesh) |
| Electrode | $35 \times 37.8 \times 37.8 \mu\text{m}^3$ |
| Current collector | $5 \times 37.8 \times 37.8 \mu\text{m}^3$ |
| Separator | $12 \times 37.8 \times 37.8 \mu\text{m}^3$ |
| AM 94% - CBD 6% symmetric cell dimensions | |
| Simulation Box | $121 \times 40 \times 40 \mu\text{m}^3$ (236002 tetrahedrons in mesh) |
| Electrode | $49.5 \times 40.1 \times 40.1 \mu\text{m}^3$ |
| Current collector | $5 \times 40.1 \times 40.1 \mu\text{m}^3$ |
| Separator | $12 \times 40.1 \times 40.1 \mu\text{m}^3$ |
| Electrolyte properties | |
| Concentration | 10 mM |
| Bulk ionic conductivity | $3.749 \times 10^{-2} \text{ S m}^{-1}$ [measured] |
| Diffusion coefficient | $7.5 \times 10^{-11} \text{ m}^2 \text{ s}^{-1}$ [32] |
| NMC properties | |
| Bulk electrical conductivity | $1.06 \times 10^{-3} \text{ S m}^{-1}$ [33] |
| CBD properties | |
| Bulk electrical conductivity | 760 S m^{-1} [34] |
| Surface double layer capacitance | 0.2937 F m^{-2} [31,35] |
| Aluminum current collector properties | |
| Bulk electrical conductivity | $3.774 \times 10^7 \text{ S m}^{-1}$ [31] |
| Separator properties | |
| Porosity | 40% |

4. Results and discussion

4.1. Parameters influencing on the EI spectrum shape

Nyquist and Bode plots for the experimental NMC 96% - C 2% - PVdF 2% electrode are displayed in Fig. 2 A and B, respectively. There are three different regions with characteristic impedance behavior: an almost vertical straight low frequency ($<1 \text{ Hz}$), a sloping mid frequency ($1-10^2 \text{ Hz}$) and a curved high frequency ($>10^3 \text{ Hz}$) region. The low frequency part, which has a phase angle $\sim 65^\circ$ (slope = 77°), corresponds to the double layer formation in the electrolyte-electrode interface. Surface roughness or an inhomogeneous current distribution alter the ideally polarizable behavior of the electrodes, rendering phase angles lower than 90° for capacitive phenomena [36,37]. The second sloping mid-frequencies region has an angle ranging from 25 to 18° (slope = 32°) and is associated to the electrolyte ionic resistance within the porous electrode, as in this frequency zone the penetration length is in the order of the ion diffusion length [11]. Furthermore, since the blocking electrolyte ensures that no faradaic current is flowing during the EI experiment, the high frequency curved EI response cannot be related to charge transfer processes. Nevertheless, TLM predicts a 45° slope and no semi-circle even in the high-frequency limit. The origin of these deviations has been studied in last years by many authors and several hypotheses have been proposed. Among them we can highlight the contact resistance between the electrode and the current collector [5,38], the anomalous electronic transport effects in the conductive carbon phase within the porous electrode mesostructure [39], the homogeneous [9] and heterogeneous [7,40] pore size distribution and the different pore shapes [11], the hierarchical organization of macro-/meso-/microporosity [8,10], and the non-uniform current distribution over the pore section (resulting in smaller virtual pore radii, compared to the real pore dimensions) [41]. Here, with the help of our 4D-resolved simulations, we shed light to this issue.

Nyquist and Bode phase plots of the simulated AM 96% - CBD 4% electrode are displayed in Fig. 2C and D, respectively. By comparing

with the experimental Bode phase plot it can be seen that both profiles are very similar in terms of shape, although in simulated spectra the characteristic frequencies are shifted towards higher values. This is due to the fact that all electronic/ionic phenomena within the simulated electrode occurs faster than the experimental one. Furthermore, the mid frequency region (with a 32° slope) is shorter than the experimental one, which is related to the small size of the electrode slab used in the simulation. To reduce the calculation time, we worked with electrode slabs of $38.8 \mu\text{m}$, which makes a total cell thickness of $99.6 \mu\text{m}$, while the typical thickness of an experimental symmetric cell is around $416 \mu\text{m}$. Thinner electrodes means shorter ionic paths for conduction rendering smaller R_{ion} . Experimental EI spectrum for a symmetric cell with a thinner electrode ($43 \mu\text{m}$) confirms this (Fig. S5), rendering only a curved response in the mid-to-high frequency region. The low frequency part in the simulated spectra is parallel to the imaginary axis and has $\sim 90^\circ$ phase angle as the interfaces were treated as ideally polarizable.

Fig. 3A and B shows the ionic (electrolyte within the pores and CBD) and electronic (NMC and CBD) contribution to the total impedance of a cross-sectional cut at half the electrode thickness. Panel C depicts the location of CBD, AM and pores phases for reference. The cross-sectional 2D plots for the ionic contribution to the impedance from 10^3 to 10^5 Hz reveal that the impedance on the electrolyte is very low and almost constant while the ionic contribution in the CBD phase increases with the frequency. This is related to the fact that the penetration depth sampled by the alternating signal grows with the frequency and therefore the concentration of the ionic species penetrates deeper into the pores within the phase [11]. In our simulations, the electrolyte transport within CBD pores is modelled with effective diffusion and ionic conductivity coefficients $D_{\text{el}}^{\text{eff}}$ (Eq. (10)) and $\sigma_{\text{el}}^{\text{eff}}$ (Eq. (11)), respectively. In this sense, the 3D explicit consideration of CBD phase with a different physics than the one adopted for the AM particles enables a detailed analysis of the electrochemical phenomena, in contrast to all the previously reported models [17,18,42,43].

As stated above, the high-frequency curved region (which can be seen both in the experimental and simulated EI spectra) was linked, among others, to the current collector-electrode contact resistance [3], AM-CBD contact resistance or anomalous electronic transport [39]. Within the formalism of our model there is no contact resistance between the current collector and the electrode and between the AM and CBD phases so these possibilities can be excluded.

To further understand the phenomena associated to the curved high frequency region we focus the analysis on the properties of the CBD phase. Namely, the physics behind CBD phase will be changed in order to understand its impact on the EI spectra. Fig. 4 A and B present the Nyquist and Bode plots, respectively, for the simulated AM 96% - CBD 4% in the cases of 100% solid CBD particles and with 20% of its volume fraction accessible to the electrolyte, with and without the Bruggeman correction of σ_{el} and D_{el} (Fig. S6 displays a scheme of the different physics taken into account, for better comprehension). When considering a 100% solid CBD phase, the high frequency curved region increases its size. In the case of the CBD that can be accessed by the electrolyte and without Bruggeman correction, the high frequency curved region decreases its size and tends to be more straight line-like with a slope equal to 25° . In terms of the total accessible volume to the electrolyte, the 100% solid CBD case has $3.37 \times 10^{-14} \text{ m}^3$ while for the electrolyte-accessible CBD the volume is $3.56 \times 10^{-14} \text{ m}^3$. Therefore, upon reducing the volume accessible to the electrolyte the high-frequency region tends to curve. Moreover, when comparing the 20% inner-porous CBD phase (same accessible electrolyte volume) the effective Bruggeman correction outputs smaller $\sigma_{\text{el}}^{\text{eff}}$ and $D_{\text{el}}^{\text{eff}}$ which in time makes the high frequency region to curve.

The 2D ionic contributions to the impedance heat maps of Fig. 4C reveal that, for the same frequency (in the range between $10 - 10^5 \text{ Hz}$), the impedance of the electrolyte in the pore regions remains unchanged. The main changes are seen in the electrolyte within the CBD phase. For

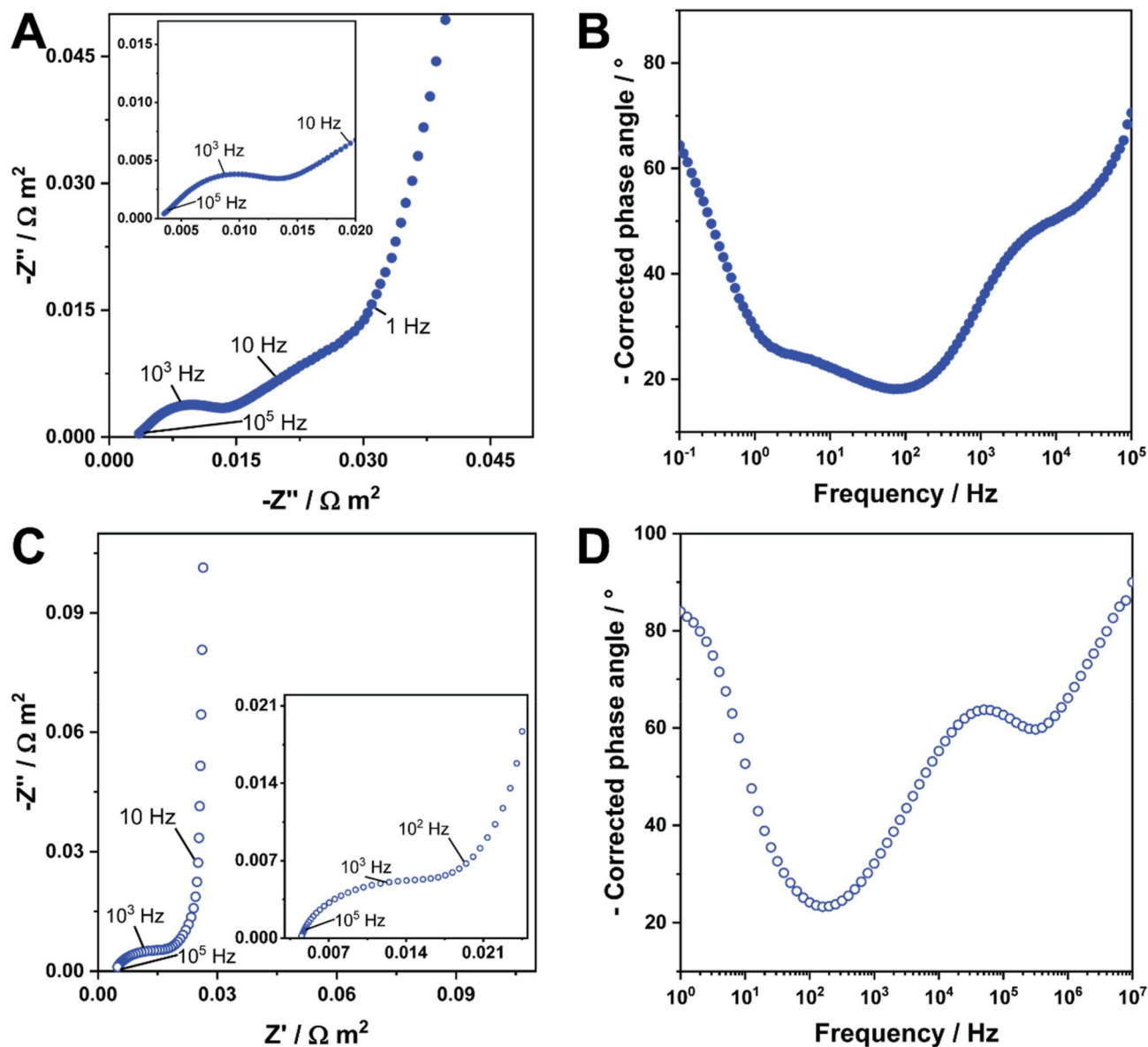


Fig. 2. Experimental (A, B) and simulated (C, D) Nyquist (A, C) and Bode (B, D) plots of a NMC 96% - C 2% - PVdF 2% and NMC 96% - CBD 4% symmetric cell, respectively.

the 10^4 and 10^5 Hz 2D plots, the ionic contribution to the impedance is higher for the Bruggeman corrected CBD phase. Summing up, the total volume available for electrolyte impregnation and the influence of porosity on its properties (namely, σ_{el} and D_{el}) are some of the factors that determine the presence of a curved high frequency region. The increase in total accessible volume tends to decrease the size of the curved region. On the contrary, the consideration that CBD inner porosity causes a reduction in electrolyte effective parameters, compared to its bulk σ_{el} and D_{el} , generates the opposite effect.

It is generally considered that the effect of the solid phases conductivity on the high to middle frequencies is almost non-existent, especially if a diluted electrolyte is used for the symmetric cell experiments [44]. Fig. S7 A and B depict the Nyquist and Bode plots, respectively, for the simulated AM 96% - CBD 4% with different values of CBD and NMC phases conductivities (K_{CBD} and K_{NMC} , respectively): 760 and 1.06×10^{-3} , 760 and 1.06×10^{-5} , and 0.076 and $1.06 \times 10^{-3} \text{ S m}^{-1}$. The decrease in K_{NMC} at constant K_{CBD} (green vs. black dotted curves in Fig. S7) causes the Nyquist plot to curve in the low frequency region while the sloping mid frequency region reduces its size. The decrease of

K_{CBD} at constant K_{NMC} (violet vs. black dotted curves in Fig. S7) makes the high frequency intercept on the real axis to upshift, while the curved region reduces its size and flattens, with a slope of 20° . Furthermore, the characteristic frequency of the curved region downshifts to lower values. All the above indicates that solid phase properties also shape the EI response. The charge balance equations ensure that the ionic current coming from the electrolyte in the pores and CBD is counterbalanced by the electronic charge coming from the CBD and NMC phases. The decrease in their conductivities causes a change in the kinetics of the double layer formation which produces an increase in the frequency. The latter can also be seen in the cross-sectional 2D plots corresponding to the ionic contribution to the total impedance, depicted in panel C of Fig. S7.

To compare the influence of electrolyte conductivity on the EI response, simulations were done at various electrolyte concentrations (*i. e.* at different σ_{el}) and are shown in Fig. 5 A and B. As the electrolyte conductivity decreases from 0.473 S m^{-1} to 4.19×10^{-3} the high-to-mid frequency region evolves to a more curved profile while its characteristic frequency downshifts. Furthermore, the high frequency intercept on the

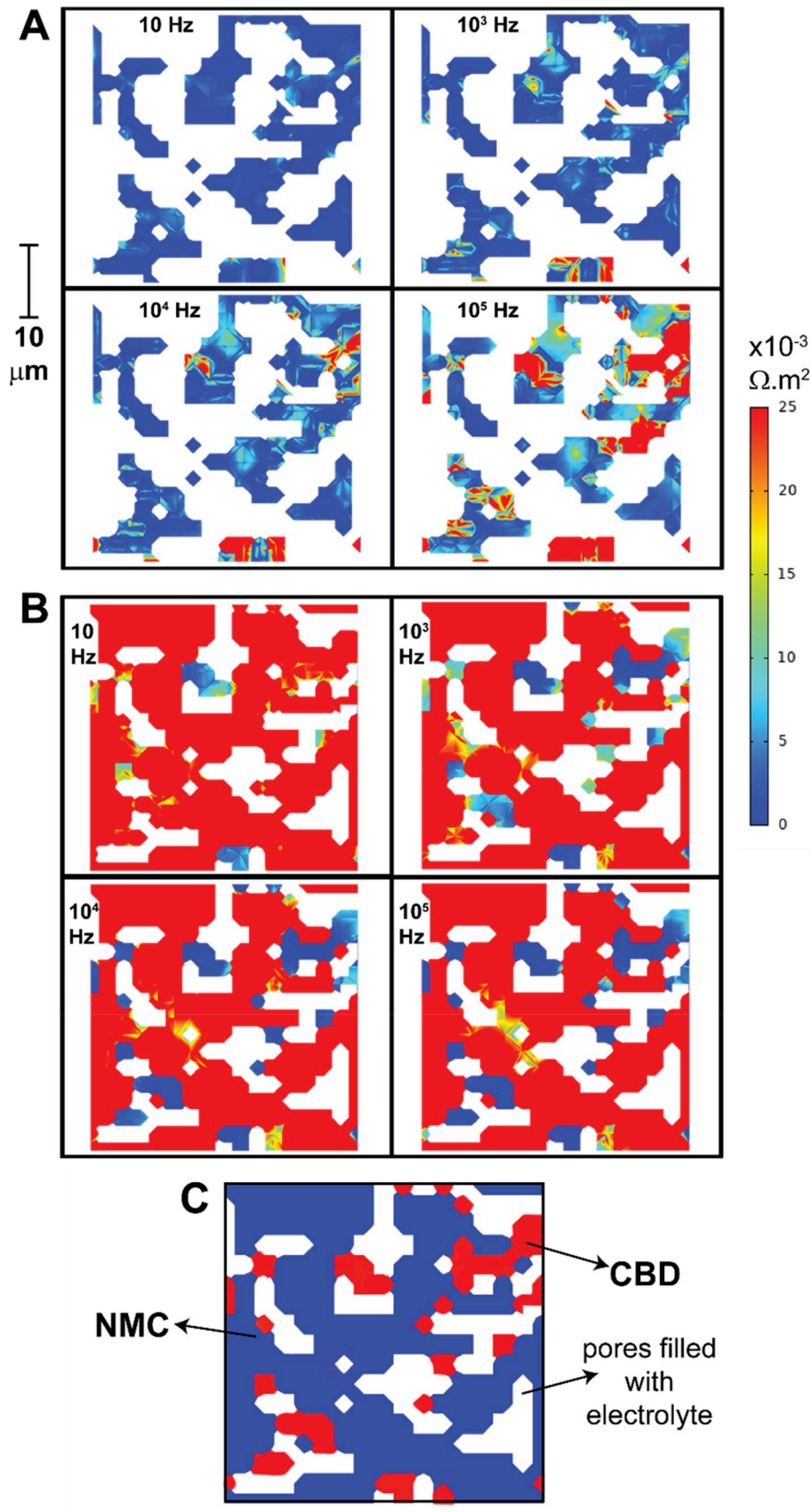


Fig. 3. Simulated NMC 96% - CBD 4% electrode cross-sectional impedance 2D plots corresponding to the ionic (A) and electronic (B) contribution to the total measured impedance, at selected frequency values. Note that due to our model formality, impedance on CBD phase appear in both ionic and electronic 2D plots. (C) Scheme of the cross-section cut, where each phase is explicitly tagged with different colors. The cut-views were done at half the electrode thickness. (For interpretation of the references to color in this figure legend, the reader is referred to the Web version of this article.)

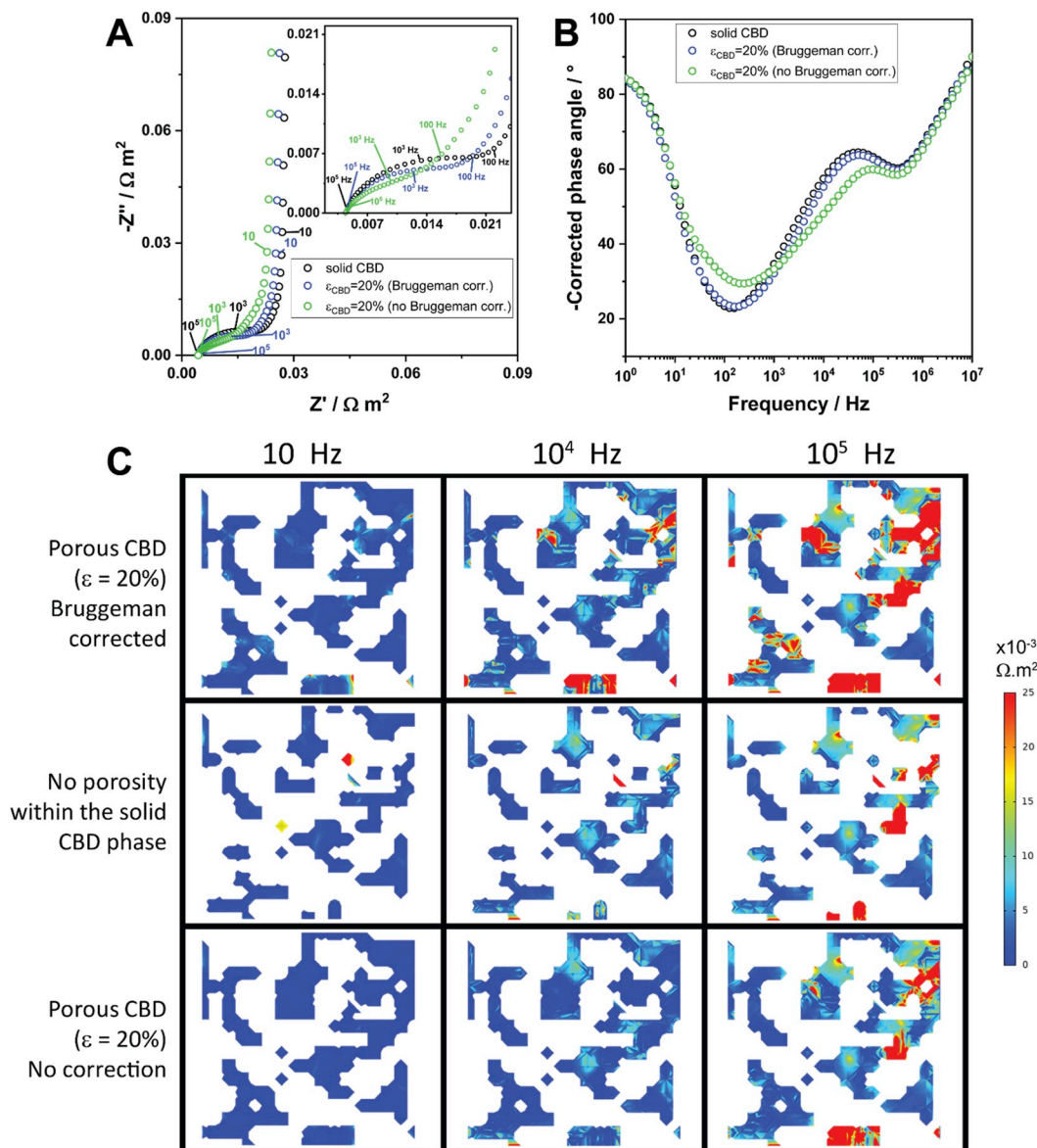


Fig. 4. Simulated Nyquist (A) and Bode (B) plots for NMC 96% - CBD 4% symmetric cell, in which CBD is treated as a solid non-porous phase (black circles) and 20% porous CBD with σ_{el} and D_{el} equal to their bulk values (green circles) and with Bruggeman-corrected σ_{el}^{eff} and D_{el}^{eff} . (C) Electrode cross-sectional impedance 2D plots corresponding to the ionic contribution to the total measured impedance, at selected frequency values. The scheme of the cross-section cut is the same as in Fig. 3C. (For interpretation of the references to color in this figure legend, the reader is referred to the Web version of this article.)

real axis decreases as σ_{el} grows. This value represents the electrolyte resistance within the separator and has an inversely proportional relation with σ_{el} (section 7 in the Supporting Information) [12]. In this sense, the tortuosity factor of the separator (τ_{sep}) can be extracted from the slope of a high frequency real axis intercept vs. electrolyte resistance plot (Fig. S8). In our case, $\tau_{sep} = 3.8$ which is in good agreement with the expected values of tortuosity for commercially available separators [3, 28]. The occurrence of the curved region in the high-to-mid frequency region can be interpreted by analyzing the electrode cross-sectional impedance 2D plots corresponding to the ionic contribution to the total measured impedance depicted in panel C of Fig. 5. At constant frequency, as the concentration of the electrolyte increases, the ionic contribution to the total impedance reduces its value. Furthermore, while at 200 mM ionic contribution remains very low in all the reported frequencies, at 10 mM the main increase at high frequencies comes from the electrolyte within the CBD. When $C_{electrolyte} = 1 \text{ mM}$, and compared

to the 10 mM at 10^4 Hz , the ionic contribution comes from the electrolyte in the electrode and not exclusively from the one within the CBD phase, with effective properties lower than the bulk ones.

All the previous analyses performed on the general shape of the simulated EI spectra suggests that the ionic resistance region depends not only on the effective value of the electrolyte conductivity within the porous electrode but also in the characteristic times at which each region of the porous electrode is accessed as a function of the frequency. For the case of NMC cathodes, the low K_{NMC} values makes the system extremely sensitive to the total volume accessible to the electrolyte, K_{CBD} and the impact of CBD microporosity (which in our simulations was modelled through a Bruggeman correction of σ_{el} and D_{el}). Some studies on porous electrodes have pointed out that not all the electrolyte accessible volume can be sampled within the same time frame and the characteristic frequencies will depend upon the distribution of σ_{el}^{eff} and D_{el}^{eff} and the conductivity of the solid phases [45,46]. The diffusion rates of ions into

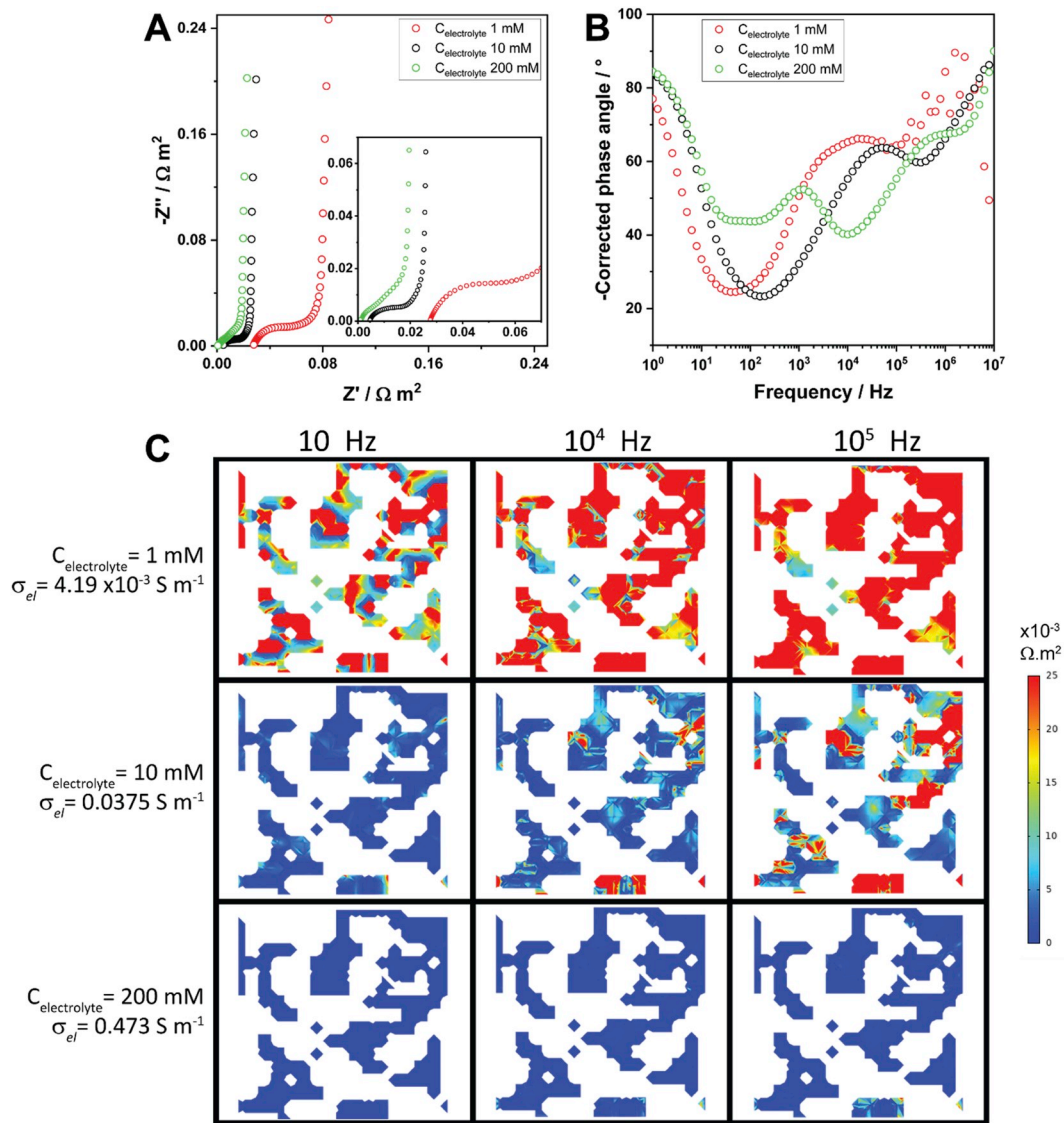


Fig. 5. Simulated Nyquist (A) and Bode (B) plots for NMC 96% - CBD 4% symmetric cell, for different TBAClO₄ electrolyte concentrations: 1 mM ($\sigma_{el} = 4.19 \times 10^{-3} \text{ S m}^{-1}$, red dots), 10 mM ($\sigma_{el} = 0.0375 \text{ S m}^{-1}$, black dots) and 200 mM ($\sigma_{el} = 0.473 \text{ S m}^{-1}$, green dots). (C) Electrode cross-sectional impedance 2D plots corresponding to the ionic contribution to the total measured impedance, at selected frequency values, for each of the EI spectra of panels A and B. The scheme of the cross-section cut is the same as in Fig. 3C. (For interpretation of the references to color in this figure legend, the reader is referred to the Web version of this article.)

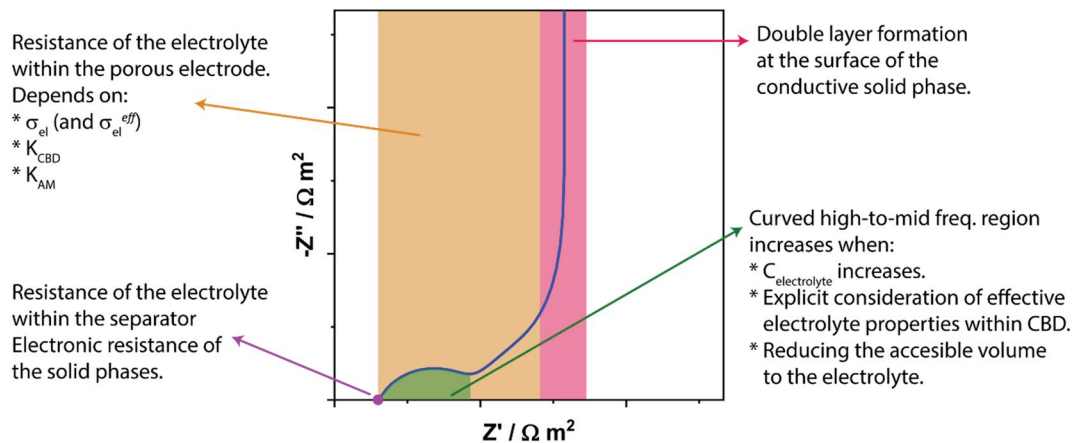


Fig. 6. Schematic Nyquist plot showing the contribution of the electrolyte and solid phases parameters on the different regions of the EI spectrum.

and within the different electrode moieties with different effective parameters will vary with the frequency, which directly impacts the response times of the double layers established on the surface of the pores.

Fig. 6 presents a summary of the found contributions of each parameter to the EI spectra of symmetric cell NMC cathodes. Our time resolved 3D electrochemical model with explicit consideration of AM and CBD phases allows to analyze in a systematic way the impact of each phase properties on the EI spectrum features. The versatility of it resides in the fact that no assumptions were made on the conductivity of the solid phase (unlike the reported works with equivalent electric circuits) and the possibility of considering different ion/electric transport regimes in the different electrode phases (as opposed to the Newman time-resolved simulations with homogenization of the solid phase).

4.2. Effect of AM amount and tortuosity factor calculations

Fig. 7 presents the experimental (A, B) and simulated (C, D) Nyquist and Bode spectra for symmetric cells with different AM/CBD compositions: NMC 96% (black dots), NMC 95% (red dots) and NMC 94% (blue dots). Regardless the fact that the simulated spectra do not exactly reproduce the experimental spectra, as simulated symmetric cells are thinner than the experimental ones, the main features resemble and the trends as a function of the electrode composition are maintained. In both the experimental and simulated EI response it can be seen that the

Table 3

Selected geometric features of the simulated electrodes at the three NMC compositions.

| Composition | Percentage of electrolyte volume within the CBD phase(%) ^a | Volume fraction accessible to the electrolyte(%) ^b | τ_{diff}^c |
|------------------|---|---|-----------------|
| NMC 96% - CBD 4% | 5.3 | 34.0 | 1.54 |
| NMC 95% - CBD 5% | 6.3 | 34.7 | 1.60 |
| NMC 94% - CBD 6% | 7.1 | 36.3 | 1.61 |

^a Calculated as the ratio between the CBD volume accessible to the electrolyte and the total volume of the electrode.

^b Calculated as the ratio between the total volume accessible to the electrolyte (CBD + pores) and the total volume of the electrode.

^c Calculated with GeoDict®.

sloping and curved mid-to-high frequency parts reduce their size and the frequencies of the different phenomena upshift when going from NMC 96% to NMC 94% electrodes. Furthermore, the cross-sectional views of the three different NMC composition electrode for the ionic contribution to the total impedance (Fig. S9) show that as the frequency increases, the impedance is higher for the electrolyte inside the porous CBD phase.

Table 3 shows that the volume fraction accessible to the electrolyte

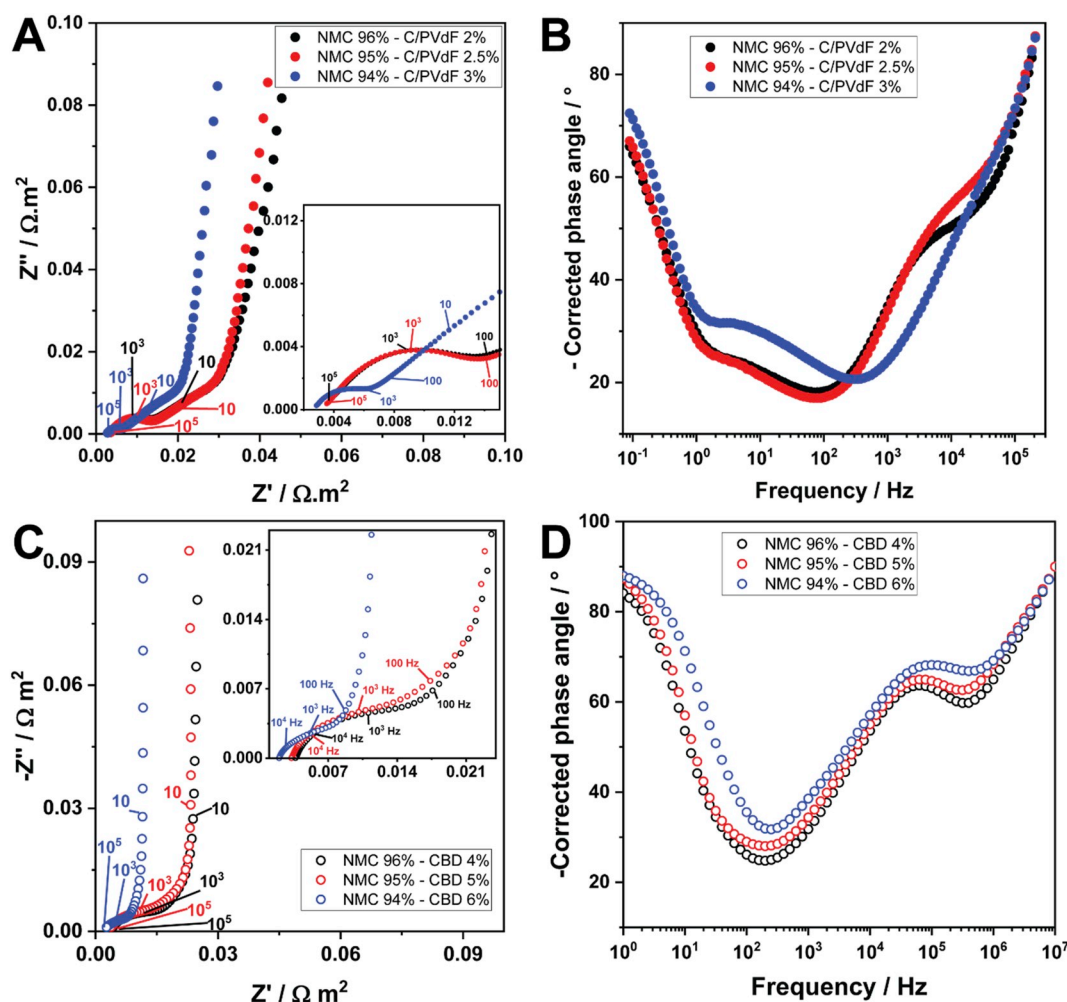


Fig. 7. Experimental (A, B) and simulated (C, D) Nyquist (A, C) and Bode (B, D) plots of a NMC 96% - C 2% - PVdF 2%/NMC 96% - CBD 4% (black dots), NMC 95% - C 2.5% - PVdF 2.5%/NMC 95% - CBD 5% (red dots) and NMC 94% - C 3% - PVdF 3%/NMC 94% - CBD 6% (blue dots) symmetric cell, respectively. (For interpretation of the references to color in this figure legend, the reader is referred to the Web version of this article.)

increases with the amount of CBD in the electrodes. As shown in Fig. 6, the reduction in the curved high frequency region is related to the increase in the accessible volume for the electrolyte. Furthermore, when comparing NMC 96%–95% high frequency intercept on the real axis to the one in NMC 94% electrode the drastic reduction in this value is due to the higher amount of conductive CBD phase which also causes an upshift in the frequency of the processes (Bode plot of Fig. 7 D). However, the increase in the CBD amount would also increase the ionic impedance contribution due to higher contributions of the lower effective values σ_{el}^{eff} and D_{el}^{eff} , as seen in the second column of Table 3. We determined above that the fact of performing a Bruggeman correction to the electrolyte properties within the CBD phase causes an increase in the curved high frequency region. In this case, we see the opposite behavior when decreasing the amount of NMC in the simulated electrode because the effect that dominates is the increase in the electrode conductivity as a consequence of the higher amount of CBD conducting phase.

The fact that the mid-to-high frequency region is due only to ionic transport within the porous medium comes from the assumption that electrolyte ionic resistance is at least two orders of magnitude higher than solid electrode electronic resistance. Recently, Landesfeind et al. [44] pointed out that if this condition is not met, then both of the conducting phenomena will play a role in the total resistance measured by impedance. To corroborate this condition, $\sigma_{electronic}$ of the experimental NMC electrodes soaked with the 10 mM TBAClO₄ electrolyte were measured. Table 4 presents these values for the three experimental NMC electrodes, along with the ionic resistances (calculated by the graphical method proposed by Landesfeind et al. using EI data [3]). The calculated $R_{ion}/R_{electronic}$ show that for the NMC 96% electrode the ratio is smaller than 100 which would imply that the effective electrolyte conductivity cannot be derived from the EI spectra. Furthermore, and although for NMC 95% and 94% this condition is met, the appearance of the curved high-to-mid frequency feature and the fact that the mid frequency part has a slope of 34° points out that the TLM cannot be used to calculate the tortuosity factors as the conditions for applying it are not met. Once again, the complex interplay between the pore size distribution (and its impact in the electrolyte effective parameters) and the different conductivities for the solid phase generates a distribution in the frequencies at which the ionic resistance of the electrolyte is sampled. Furthermore, the calculated values of τ_{EIS} do not follow a clear trend when increasing the amount of conductive carbon and binder. It is expected that τ should increase when going from NMC 96% to NMC 94% as a result of: (i) adding more conductive carbon and the consequent increase in the electrode microporosity; and (ii) adding more binder, which would generate thicker layers of polymer over the solid particles [3,13,14,47].

To fully compare the τ coming from EI experiments with the ones calculated from the diffusivity (using DiffuDict® module of GeoDict® software on the simulated electrode structures), EI simulations were performed on thicker NMC 96% - CBD 4% cathodes. The Nyquist plot

(Figure S11 A) shows that for a 148.7 μm thick electrode the sloping mid frequency region dominates the high-to-mid frequency region (with a slope of 45°). Nevertheless, at very high frequencies the EI spectra features a curved region as in the previous thinner simulated electrodes. The comparison with the same electrode but considering a fully solid CBD (no permeability to the electrolyte) shows that in thicker electrodes the mid-to-high curved region now represents a smaller part of the Nyquist plot. For this electrode, the τ_{EIS} coming from the graphic interpolation of the impedance spectrum outputs a value of 12.5 while the τ_{diff} derived from GeoDict® software is 1.79. A straightforward way to validate if each methodology captures correctly the τ is to compare these values with an electrode which has been calendered. In this case, the application of a pressure generates a reduction in the pore size/porosity and an increase in the contacts between the conducting particles [47–49] which normally is associated with an increase in τ . For the calendered simulated NMC 96% - CBD 4% cathode (Fig. S11) $\tau_{EIS} = 4.6$ while $\tau_{diff} = 1.84$ (further details on the generation of the calendered simulated structure and τ calculations can be found in section 1 and 2 in the Supporting Information, respectively). The τ_{diff} shows the expected trend whereas τ_{EIS} does not. Note also that τ_{diff} successfully disclosed the rise in the tortuosity for the electrodes with increasing amount of CBD (fourth column of Table 3 for the simulated electrodes NMC 96%, NMC 95% and NMC 94%). As a general remark, it is expected that τ_{diff} outputs lower tortuosity factors than the EIS-based method, as it does not take into account the inner CBD porosity.

All the above points out the complexity of the phenomena that determines the impedance response of electrode pores filled with a diluted, non-intercalating electrolyte. The approximation that the electrolyte effective ionic conductivity can be derived from the mid-to-high frequency region works only if one effective parameter comes out of the measured response. Our physical model for the calculation of EI spectra in three-phase simulated electrodes enabled to understand that the physics that explains the observed response is not as simple as a decrease in the electrolyte effective properties. This comes from the fact that NMC phase is a poor electronic conductor that represents 60%, 57% and 53% of the electrodes total volume for NMC 96%, 95% and 94%, respectively. In this sense, the electron conduction takes place mainly at the CBD phase, which in time has inner porosity that constraints the electrolyte effective properties. Furthermore, the TLM model assumes no limitations on the solid electronic conductivity, while it is known that conductivity in porous media depends on the percolation and spatial distribution of the conductive particles [50]. Therefore, this kind of systems are quite sensitive to the spatial location of the CBD phase and the degree at which the latter affects the electrolyte properties. It is not surprising then that the reported electrodes at which EIS methodology was used to derive the electrode tortuosity factor are mainly graphite-based anodes [3,12–14]. In the latter, both the carbon additive and the AM are good electronic conductors so there are no limitations on the solid phase side in terms of the electronic conductivity.

As it has been discussed in Cooper et al. work [51], there is still much debate around the best way to acquire a representative τ value for porous electrodes. In this work we discussed EIS-based technique but the most widely used methodologies, such as geometric- and diffusivity-derived, lack of information regarding to microporosity (as they rely on tomography results for the calculation) and they are highly anisotropic (meaning that they can measure τ either in the x, y or z direction of the electrode structure) [47].

5. Conclusions

In this work, a 4D (3D in space + time) physical model was successfully used to simulate and analyze EI spectra of symmetric cells based on simulated NMC cathodes for the evaluation of their tortuosity factor. The results were compared and validated with experimental *in house* EI spectra acquired on real NMC cathodes. The electrochemical 4D model explicitly considers the three electrode phases (*i.e.* AM and CBD

Table 4

Solid phase electronic conductivities ($\sigma_{electronic}$), ionic resistances (R_{ion}) of the electrolyte within the electrode pores, $R_{ion}/R_{electronic}$ ratios and tortuosities (τ_{EIS}) calculated according to Landesfeind et al. [3].

| Composition | $\sigma_{electronic}/S\ m^{-1a}$ | $R_{ion}/\Omega\ m^{2b}$ | $R_{ion}/R_{electronic}^c$ | τ_{EIS}^d |
|-----------------------|----------------------------------|--------------------------|----------------------------|----------------|
| NMC 96% - C/PVdF 2% | 0.261 | 0.0815 | 60 | 3.93 |
| NMC 95% - C/PVdF 2.5% | 0.521 | 0.0799 | 127 | 4.08 |
| NMC 94% - C/PVdF 3% | 0.785 | 0.0512 | 122 | 2.87 |

^a Measured.

^b Obtained from the graphical interpolation of the high-to-mid frequency region on the experimental EI spectra (Fig. S10, in the Supporting Information).

^c $R_{electronic}$ was obtained as $\ell/\sigma_{electronic}$, where ℓ is the electrode thickness.

^d EIS-derived tortuosity factor was obtained through the graphical method according to Landesfeind et al. [3].

particles and the pores filled with electrolyte) along with distinctive physics for the electron and ion conduction within them.

In the first part of the work the general features of the EI were discussed: Fig. 6 provides a good summary of them. It was found that, unlike TLM used for the interpretation of spectra, the high-to-mid frequency region deviated from a 45° slope and a curved region at high frequency appears, both in simulated and experimental cases. The possibility of analyzing each electrode parameter at a time enabled to conclude that these deviations from the “ideal TLM” are related to the characteristic times at which each region of the porous electrode is accessed as a function of the frequency. The fact that our model considers a Bruggeman-corrected ion diffusion/conduction of electrolyte within the porous CBD phase and different electronic conductivities for AM and CBD, proved to be a successful strategy for the interpretation of EI spectra in symmetric cells.

In the second part, the main limitations for the calculation of NMC-based cathodes τ from symmetric cell-EI experiments were analyzed. The comparison of electrodes with different NMC/CBD compositions both simulated and experimental revealed that τ_{EIS} , which comes from the electrolyte effective ionic conductivity, output values and trends which are not the expected ones. Although all the methodologies for the

τ calculation have their limitations and assumptions, for the case of porous electrodes in which the AM is not a good electronic conductor, EI-symmetric cell may output erroneous results. Nonetheless, our 4D explicit model helped to understand this matter as we could compare τ values coming from two independent methodologies for the same electrode structure.

Declaration of competing interest

The authors declare that they have no known competing financial interests or personal relationships that could have influenced the work reported in this paper.

Acknowledgements

The authors acknowledge the European Union's Horizon 2020 research and innovation programme for the funding support through the European Research Council (grant agreement 772873, “ARTISTIC” project). A.A.F. also acknowledges Institut Universitaire de France for the support.

Appendix A. Supplementary data

Supplementary data to this article can be found online at <https://doi.org/10.1016/j.jpowsour.2020.227871>.

Nomenclatures

| | |
|--------------------|--|
| AM | Active material |
| C | Carbon black |
| CBD | Carbon-binder domain |
| CGMD | Coarse-grained molecular dynamics |
| j | Current density |
| D | Diffusion coefficient |
| A_{dl} | Double layer area |
| C_{dl} | Double layer capacitance |
| j_{dl} | Double layer current density |
| eff | Effective value |
| EIS | Electrochemical impedance spectroscopy |
| ℓ | Electrode thickness |
| C_{el} | Electrolyte concentration |
| ε_{el} | Electrolyte volume fraction within CBD |
| K | Electronic conductivity |
| F | Faraday's constant |
| N | Flux density |
| f | Frequency |
| σ | Ionic conductivity |
| R_{ion} | Ionic resistance |
| i | i th species |
| NMC | $\text{Li}(\text{Ni}_{1/3}\text{Mn}_{1/3}\text{Co}_{1/3})\text{O}_2$ |
| N_M | MacMullin number |
| MD | Molecular dynamics |
| \mathbf{n} | Normal vector |
| PVdF | Polyvinylidene fluoride |
| ε | Porosity |
| φ | Potential |
| T | Temperature |
| t | Time |
| τ | Tortuosity factor |
| TLM | Transmission line model |
| R | Universal gas constant |
| α | Variable |
| a_0 | Variables solution for the average field |
| $j_{V,dl}$ | Volumetric double layer current density |

References

- [1] D. Castelvocchi, E. Stoye, Chemistry Nobel honours world-changing batteries, *Nature* 574 (2019), <https://doi.org/10.1038/d41586-019-02965-y>, 308–308.
- [2] B. Tjaden, D.J.L. Brett, P.R. Shearing, Tortuosity in electrochemical devices: a review of calculation approaches, *Int. Mater. Rev.* 63 (2018) 47–67, <https://doi.org/10.1080/09506608.2016.1249995>.
- [3] J. Landesfeind, J. Hattendorf, A. Ehrl, W.A. Wall, H.A. Gasteiger, Tortuosity determination of battery electrodes and separators by impedance spectroscopy, *J. Electrochem. Soc.* 163 (2016) A1373–A1387, <https://doi.org/10.1149/2.1141607jes>.
- [4] R. Zahn, M.F. Lagadee, V. Wood, Transport in lithium ion batteries: reconciling impedance and structural analysis, *ACS Energy Lett.* 2 (2017) 2452–2453, <https://doi.org/10.1021/acseenergylett.7b00740>.
- [5] F. Pouraghajan, H. Knight, M. Wray, B. Mazzeo, R. Subbaraman, J. Christensen, D. Wheeler, Quantifying tortuosity of porous Li-ion battery electrodes: comparing polarization-interrupt and blocking-electrolyte methods, *J. Electrochem. Soc.* 165 (2018) A2644–A2653, <http://jes.ecsdl.org/content/165/11/A2644.abstract>.
- [6] U. Tröltzsch, O. Kanoun, Generalization of transmission line models for deriving the impedance of diffusion and porous media, *Electrochim. Acta* 75 (2012) 347–356, <https://doi.org/10.1016/j.electacta.2012.05.014>.
- [7] R. Kant, M.B. Singh, Theory of the electrochemical impedance of mesostructured electrodes embedded with heterogeneous micropores, *J. Phys. Chem. C* 121 (2017) 7164–7174, <https://doi.org/10.1021/acs.jpcc.7b01287>.
- [8] M. Itagaki, Y. Hatada, I. Shitanda, K. Watanabe, Complex impedance spectra of porous electrode with fractal structure, *Electrochim. Acta* 55 (2010) 6255–6262, <https://doi.org/10.1016/j.electacta.2009.10.016>.
- [9] M. Musiani, M. Orazem, B. Tribollet, V. Vivier, Impedance of blocking electrodes having parallel cylindrical pores with distributed radii, *Electrochim. Acta* 56 (2011) 8014–8022, <https://doi.org/10.1016/j.electacta.2010.12.004>.
- [10] Q.-A. Huang, Y. Li, K.-C. Tsay, C. Sun, ChangpingYang, L. Zhang, J. Zhang, Multiscale impedance model for supercapacitor porous electrodes: theoretical prediction and experimental validation, *J. Power Sources* 400 (2018) 69–86, <https://doi.org/10.1016/j.jpowsour.2018.07.108>.
- [11] S.J. Cooper, A. Bertei, D.P. Finegan, N.P. Brandon, Simulated impedance of diffusion in porous media, *Electrochim. Acta* 251 (2017) 681–689, <https://doi.org/10.1016/j.electacta.2017.07.152>.
- [12] S. Malifarge, B. Delobel, C. Delacourt, Determination of tortuosity using impedance spectra analysis of symmetric cell, *J. Electrochem. Soc.* 164 (2017) E3329–E3334, <https://doi.org/10.1149/2.033171jes>.
- [13] J. Landesfeind, A. Eldiven, H.A. Gasteiger, Influence of the binder on lithium ion battery electrode tortuosity and performance, *J. Electrochem. Soc.* 165 (2018) A1122–A1128, <https://doi.org/10.1149/2.0971805jes>.
- [14] R. Morasch, J. Landesfeind, B. Suthar, H.A. Gasteiger, Detection of binder gradients using impedance spectroscopy and their influence on the tortuosity of Li-ion battery graphite electrodes, *J. Electrochem. Soc.* 165 (2018) A3459–A3467, <https://doi.org/10.1149/2.1021814jes>.
- [15] N. Ogiwara, S. Kawauchi, C. Okuda, Y. Itou, Y. Takeuchi, Y. Ukyo, Theoretical and experimental analysis of porous electrodes for lithium-ion batteries by electrochemical impedance spectroscopy using a symmetric cell, *J. Electrochem. Soc.* 159 (2012) A1034–A1039, <https://doi.org/10.1149/2.057207jes>.
- [16] A.A. Franco, A. Rucci, D. Brandell, C. Frayret, M. Gaberscek, P. Jankowski, P. Johansson, Boosting rechargeable batteries R&D by multiscale modeling: myth or reality? *Chem. Rev.* 119 (2019) 4569–4627, <https://doi.org/10.1021/acs.chemrev.8b00239>.
- [17] A.N. Mistry, P.P. Mukherjee, Probing spatial coupling of resistive modes in porous intercalation electrodes through impedance spectroscopy, *Phys. Chem. Chem. Phys.* 21 (2019) 3805–3813, <https://doi.org/10.1039/c8cp05109g>.
- [18] A.N. Mistry, K. Smith, P.P. Mukherjee, Secondary-phase stochastics in lithium-ion battery electrodes, *ACS Appl. Mater. Interfaces* 10 (2018) 6317–6326, <https://doi.org/10.1021/acsaami.7b17771>.
- [19] M. Chouchane, A. Rucci, A.A. Franco, A versatile and efficient voxelization-based meshing algorithm of multiple phases, *ACS Omega* 4 (2019) 11141–11144, <https://doi.org/10.1021/acsomega.9b01279>.
- [20] M. Chouchane, A. Rucci, T. Lombardo, A.C. Ngandjong, A.A. Franco, Lithium ion battery electrodes predicted from manufacturing simulations: assessing the impact of the carbon-binder spatial location on the electrochemical performance, *J. Power Sources* 444 (2019) 227285, <https://doi.org/10.1016/j.jpowsour.2019.227285>.
- [21] T. Pajkossy, R. Jurczakowski, Electrochemical impedance spectroscopy in interfacial studies, *Curr. Opin. Electrochem.* 1 (2017) 53–58, <https://doi.org/10.1016/j.coelec.2017.01.006>.
- [22] J.E. Vogel, M.M. Forouzan, E.E. Hardy, S.T. Crawford, D.R. Wheeler, B.A. Mazzeo, Electrode microstructure controls localized electronic impedance in Li-ion batteries, *Electrochim. Acta* 297 (2019) 820–825, <https://doi.org/10.1016/j.electacta.2018.11.204>.
- [23] A.C. Ngandjong, A. Rucci, M. Maiza, G. Shukla, J. Vazquez-Arenas, A.A. Franco, Multiscale simulation platform linking lithium ion battery electrode fabrication process with performance at the cell level, *J. Phys. Chem. Lett.* 8 (2017) 5966–5972, <https://doi.org/10.1021/acs.jpclett.7b02647>.
- [24] A. Rucci, A.C. Ngandjong, E.N. Primo, M. Maiza, A.A. Franco, Tracking variabilities in the simulation of Lithium Ion Battery electrode fabrication and its impact on electrochemical performance, *Electrochim. Acta* (2019), <https://doi.org/10.1016/j.electacta.2019.04.110>.
- [25] H. Zheng, R. Yang, G. Liu, X. Song, V.S. Battaglia, Cooperation between active material, polymeric binder and conductive carbon additive in lithium ion battery cathode, *J. Phys. Chem. C* 116 (2012) 4875–4882, <https://doi.org/10.1021/jp208428w>.
- [26] M. Widmaier, K. Pfeifer, L. Bommer, V. Presser, Valence-tuned lithium titanate nanopore for high-rate electrochemical energy storage, *Batter. Supercaps* 1 (2018), <https://doi.org/10.1002/batt.201800036>, 2–2.
- [27] H. Chen, M. Ling, L. Hencz, H.Y. Ling, G. Li, Z. Lin, G. Liu, S. Zhang, Exploring chemical, mechanical, and electrical functionalities of binders for advanced energy-storage devices, *Chem. Rev.* 118 (2018) 8936–8982, <https://doi.org/10.1021/acs.chemrev.8b00241>.
- [28] M.F. Lagadee, M. Ebner, R. Zahn, V. Wood, Communication - technique for visualization and quantification of lithium-ion battery separator microstructure, *J. Electrochem. Soc.* 163 (2016) A992–A994, <https://doi.org/10.1149/2.0811606jes>.
- [29] H. Wang, L. Pilon, Intrinsic limitations of impedance measurements in determining electric double layer capacitances, *Electrochim. Acta* 63 (2012) 55–63, <https://doi.org/10.1016/j.electacta.2011.12.051>.
- [30] B.A. Mei, O. Munteshari, J. Lau, B. Dunn, L. Pilon, Physical interpretations of nyquist plots for EDLC electrodes and devices, *J. Phys. Chem. C* 122 (2018) 194–206, <https://doi.org/10.1021/acs.jpcc.7b10582>.
- [31] COMSOL, Introduction to COMSOL Multiphysics 5.3, Manual (2014) 168.
- [32] M.A. Valle, A.M. Ramírez, L.A. Hernández, F. Armijo, F.R. Díaz, G.C. Arteaga, Influence of the supporting electrolyte on the electrochemical polymerization of 3, 4-ethylenedioxythiophene. Effect on p- and n-doping/undoping, *Conduct. Morphol.* 11 (2016) 7048–7065, <https://doi.org/10.20964/2016.08.46>.
- [33] Y. Chen, C. Wang, X. Zhang, A.M. Sastry, Porous cathode optimization for lithium cells: ionic and electronic conductivity, capacity, and selection of materials, *J. Power Sources* 195 (2010) 2851–2862, <https://doi.org/10.1016/j.jpowsour.2009.11.044>.
- [34] C.-F. Chen, A. Verma, P.P. Mukherjee, Probing the role of electrode microstructure in the lithium-ion battery thermal behavior, *J. Electrochem. Soc.* 164 (2017) E3146–E3158, <https://doi.org/10.1149/2.016171jes>.
- [35] D.P. Abraham, S. Kawauchi, D.W. Dees, Modeling the impedance versus voltage characteristics of LiNi_{0.8}Co_{0.15}Al_{0.05}O₂, *Electrochim. Acta* 53 (2008) 2121–2129, <https://doi.org/10.1016/j.electacta.2007.09.018>.
- [36] T. Pajkossy, Impedance spectroscopy at interfaces of metals and aqueous solutions — surface roughness, CPE and related issues, *Solid State Ionics* 176 (2005) 1997–2003, <https://doi.org/10.1016/j.ssi.2004.06.023>.
- [37] P. Córdoba-Torres, T.J. Mesquita, R.P. Nogueira, Relationship between the origin of constant-phase element behavior in electrochemical impedance spectroscopy and electrode surface structure, *J. Phys. Chem. C* 119 (2015) 4136–4147, <https://doi.org/10.1021/jp512063f>.
- [38] M. Gaberscek, J. Moskon, B. Erjavec, R. Dominko, J. Jamnik, The importance of interphase contacts in Li ion electrodes: the meaning of the high-frequency impedance arc, *Electrochim. Solid State Lett.* 11 (2008) A170–A174, <https://doi.org/10.1149/1.2964220>.
- [39] J. Bisquert, G. García-Belmonte, F. Fabregat-Santiago, A. Compte, Anomalous transport effects in the impedance of porous film electrodes, *Electrochem. Commun.* 1 (1999) 429–435, [https://doi.org/10.1016/S1388-2481\(99\)00084-3](https://doi.org/10.1016/S1388-2481(99)00084-3).
- [40] J. Huang, J. Zhang, Theory of impedance response of porous electrodes: simplifications, inhomogeneities, non-stationarities and applications, *J. Electrochem. Soc.* 163 (2016) A1983–A2000, <https://doi.org/10.1149/2.0901609jes>.
- [41] T. Sharma, T. Holm, J.A. Diaz-Real, W. Mérida, Experimental verification of pore impedance theory: drilled graphite electrodes with gradually more complex pore size distribution, *Electrochim. Acta* 317 (2019) 528–541, <https://doi.org/10.1016/j.electacta.2019.05.119>.
- [42] S. Hein, A. Latz, Influence of Local Lithium Metal Deposition in 3D Microstructures on Local and Global Behavior of Lithium-Ion Batteries, 2016.
- [43] K. Kuchler, D. Westhoff, J. Feinauer, T. Mitsch, I. Manke, V. Schmidt, Stochastic model for the 3D microstructure of pristine and cyclically aged cathodes in Li-ion batteries, *Model. Simulat. Mater. Sci. Eng.* 26 (2018), <https://doi.org/10.1088/1361-651X/aaa6da>.
- [44] J. Landesfeind, M. Ebner, A. Eldiven, V. Wood, H.A. Gasteiger, Tortuosity of battery electrodes: validation of impedance-derived values and critical comparison with 3D tomography, *J. Electrochem. Soc.* 165 (2018) A469–A476, <https://doi.org/10.1149/2.0231803jes>.
- [45] M.J. Bleda-Martínez, D. Lozano-Castelló, D. Cazorla-Amorós, E. Morallón, Kinetics of double-layer formation: influence of porous structure and pore size distribution, *Energy Fuel* 24 (2010) 3378–3384, <https://doi.org/10.1021/ef901521g>.
- [46] G. Gourdin, T. Jiang, P. Smith, D. Qu, The effects of cell assembly compression on the performance of carbon electrochemical double-layer capacitor electrodes, *J. Power Sources* 215 (2012) 179–187, <https://doi.org/10.1016/j.jpowsour.2012.04.046>.
- [47] F.L.E. Usseglio-Viretta, A. Colclasure, A.N. Mistry, K.P.Y. Claver, F. Pouraghajan, D.P. Finegan, T.M.M. Heenan, D. Abraham, P.P. Mukherjee, D. Wheeler, P. Shearing, S.J. Cooper, K. Smith, Resolving the discrepancy in tortuosity factor estimation for Li-ion battery electrodes through micro-macro modeling and experiment, *J. Electrochem. Soc.* 165 (2018) A3403–A3426, <http://jes.ecsdl.org/content/165/14/A3403.abstract>.
- [48] C. Meyer, H. Bockholt, W. Haselrieder, A. Kwade, Characterization of the calendaring process for compaction of electrodes for lithium-ion batteries, *J. Mater. Process. Technol.* 249 (2017) 172–178, <https://doi.org/10.1016/j.jmatprotec.2017.05.031>.
- [49] N. Besnard, A. Etienne, T. Douillard, O. Dubrunfaut, P. Tran-Van, L. Gautier, S. Franger, J.-C. Badot, E. Maire, B. Lestriez, Multiscale morphological and electrical characterization of charge transport limitations to the power

- performance of positive electrode blends for lithium-ion batteries, *Adv. Energy Mater.* 7 (2017) 1602239, <https://doi.org/10.1002/aenm.201602239>.
- [50] F. Cadiou, A. Etienne, T. Douillard, F. Willot, O. Valentin, J.-C. Badot, B. Lestriez, E. Maire, Numerical prediction of multiscale electronic conductivity of lithium-ion battery positive electrodes, *J. Electrochem. Soc.* 166 (2019) A1692–A1703, <https://doi.org/10.1149/2.1221908jes>.
- [51] S.J. Cooper, D.S. Eastwood, J. Gelb, G. Damblanc, D.J.L. Brett, R.S. Bradley, P. J. Withers, P.D. Lee, A.J. Marquis, N.P. Brandon, P.R. Shearing, Image based modelling of microstructural heterogeneity in LiFePO₄ electrodes for Li-ion batteries, *J. Power Sources* 247 (2014) 1033–1039, <https://doi.org/10.1016/j.jpowsour.2013.04.156>.